Int. J. Electrochem. Sci., 11 **(2016)** 7309 – 7317, doi: 10.20964/2016.09.05

International Journal of
ELECTROCHEMICAL
SCIENCE
www.electrochemsci.org

$MnFe_2O_4$ Colloidal Nanocrystal Assemblies as Anode Materials for Lithium-Ion Batteries

Yuqian Cui [1,2,*], *Fangfang Leng* [1], *Guangting Han* [1], *Guoliang Zhang* [1], *Hongliang Li* [1,*], *Peizhi Guo* [1,*], *X. S. Zhao* [1]

[1] Institute of Materials for Energy and Environment, State Key Laboratory Breeding Based of New Fiber Materials and Modern Textile, School of Materials Science and Engineering, Qingdao University, Qingdao, 266071, P. R. China
[2] School of Environmental Science and Engineering, Qingdao University, Qingdao, 266071, P. R. China
[*]E-mail: pzguo@qdu.edu.cn, guopz77@yahoo.com, bonnie_cyq@163.com, lhl@qdu.edu.cn

Received: 6 April 2016 / *Accepted:* 21 June 2016 / *Published:* 7 August 2016

Submicrometer colloidal nanocrystal assemblies (CNAs) of $MnFe_2O_4$ have been synthesized solvothermally and have been sued as the electrode materials for Lithium ion batteries. Large $MnFe_2O_4$ CNAs, which were prepared with the assistance of CH_3COONH_4, possessed the size of about 950 nm showed a larger pore size but a smaller specific surface area, compared with that of 160 nm $MnFe_2O_4$ CNAs with the help of $CH_3COONa•3H_2O$. The capacitance of MnFe-NH can reach 1200 mAh g^{-1} at the first circle at the current density of 0.1 A g^{-1}. However, the capacitances were decreased drastically under the further measurements. MnFe-Na showed about 50 mAh g^{-1} lower capacity and worse cycle stability than MnFe-NH. Cyclic voltammetry and electrochemical impedance spectroscopy profile indicated the higher electronic conductivity of MnFe-NH, thanks to the larger size of primary crystalline particle and interspace between them.

Keywords: lithium ion battery; anode materials; manganese ferrite; electrochemical properties

1. INTRODUCTION

The growing consumption of fossil fuel and the deterioration of environment have urged people to develop the renewable and clean energy in large scale. In the meantime, energy storage and conversion systems are in urgent need [1,2]. Lithium-ion batteries (LIBs) are considered as an promising solution to solve the energy shortage issue duo to excellent electrochemical performance, inherent clean characteristics and versatility, which have been used in numerous fields such as computers and cell phones [3-5]. The utilization of the LIBs largely depends on the electrochemical performance of the electrodes. That is why plenty of efforts have been payed on fabricating electrode

materials with good durability, high energy density and safety. As a traditional anode material, graphite can provide capacity of 372 mAh g^{-1} theoretically [6-8]. However, the low theoretical capacity and poor cycle property constrain its application in lithium-ion battery.

Several works have reported that transition metal oxides can be anode material substitutes, such as Fe_2O_3 [9,10], NiO [11], MnO_2 [12] and CuO [13]. However, their huge volume change during cycling process and poor electric conductivity hindered their applications in LIBs [14]. Since Chen and co-workers first reported that the spinel-structured transition metal ferrites could be used as anode materials for LIBs [4,15], growing attention has been payed on these materials, including $NiCo_2O_4$ [16,17], $NiFe_2O_4$ [18-20], $ZnMn_2O_4$ [21] and $ZnFe_2O_4$ [22,23]. Among them, Fe-based oxides with spinel lattice structure have been mostly studied for their abundant resources and environmental benignity [18,24,25]. The spinel-structured ferrite materials MFe_2O_4 (M = Zn, Mn, Co, Mg, etc) can tune the energy density and working voltages by changing the M^{2+} element, and thus can provide high capacity, excellent cycling and rate performance [26]. Besides, these materials can store Li^+ through the conversion reaction ($MFe_2O_4 + 8Li^+ + 8e^- \rightarrow M + 2Fe + 4Li_2O$), which furtherly ensure the high specific capacity [20,27,28]. Nevertheless, Manganese ferrite ($MnFe_2O_4$) has not been widely studied so far though possessing high theoretical capacity of 928 mAh g^{-1}.

Research results have shown that the properties of electrode materials largely depend on their structure, size, morphology and composition. MFe_2O_4 with various morphologies has been fabricated, such as cubic and tetragonal $CuFe_2O_4$ [29], $CuFe_2O_4$ nanofibers [30], hollow spherical $ZnFe_2O_4$ and $ZnFe_2O_4$ nanodiscs [22,31]. Moreover, micrometer- and nanometer-sized materials with a spherical morphology are optimal because micro- and nano-spheres have high packing density, and accordingly high power density. Moreover, spheres have good particle mobility which is good for the formation of compact and uniform electrode layer [15,27,32]. Recently, reports indicated that nanomaterials can effectively contain the strain caused by the volume change during charge and discharge process to alleviate the pulverization problem, coupled with improve electron and Li^+ conduction [17,33,34].

Herein, we report the electrochemical performance of $MnFe_2O_4$ colloidal nanocrystal assemblies (CNAs) as an anode material for LIBs. It is found that the MnFe-NH CNAs, with larger primary particle size and the assembly diameter, possessed better cycling stability, higher capacity and lower resistance than the MnFe-Na CNAs. These conclusions imply the vital role of particle size in the electrochemical properties of manganese ferrite.

2. EXPERIMENTS

2.1 Materials

Chemicals, including $FeCl_3 \cdot 6H_2O$, $Mn(Ac)_2 \cdot 4H_2O$, CH_3COONH_4, $CH_3COONa \cdot 3H_2O$, ethyleneglycol (EG), ethanol were of analytical grade (Sinopharm Chem. Rea. Co.) and used as received. Acetylene black, polyvinylidiene fluoride (PVDF) and N-methylpyrrolidone, and polypropylene film (Celgard 2400), were purchased from Strem Chemicals, Aldrich and Tianjin Jinniu Power Sources Mater. Co., LTD, respectively.

2.2 Synthesis of $MnFe_2O_4$ colloidal nanocrystal assemblies

In a typical synthesis, $FeCl_3$•$6H_2O$ and $Mn(Ac)_2$•$4H_2O$ in a stoichiometric ratio of 2:1 were dissolved in 30 mL of ethylene glycol solution contained in a 40 ml teflon-lined autoclave under magnetic stirring at room temperature. After the solution became clear, CH_3COONH_4 (30 mM) or CH_3COONa•$3H_2O$ (10 mM) was added under stirring. Then, the homogeneous solution was sealed and heated at 200 ºC for 12 h in an oven [35,36]. Subsequently, the solid powders were collected by centrifugation, washed separately with distilled water and ethanol for several times, and then dried in an oven at 60 ºC for 8 h. The products synthesized with CH_3COONH_4 and CH_3COONa•$3H_2O$ were denoted as MnFe-NH and MnFe-Na, respectively.

2.3 Structure characterization

TEM images of the samples were recorded on a transmission electron microscope (JEM-2000EX) with an operating voltage of 120 kV. The specific surface areas were estimated by the BET method, and the pore size distribution was determined by the BJH method using a TriStar 3000 surface area and pore analyzer (Micromeritics) [35,36].

2.4 Electrochemical measurements

The electrochemical properties were characterized by using 2016 coin-type half cells assembled in an Ar-filled glove box at room temperature. The assembly of half cells and electrodes was similar to our recent report [37]. In brief, the anode was prepared by mixing the $MnFe_2O_4$ CNAs, acetylene black, and PVDF (8:1:1 by weight) in N-methylpyrrolidone. The cell was composed of the electrode and metallic lithium cathode separated by polypropylene film with 1 M $LiPF_6$ in a mixed solvent as the electrolyte with the volume ratio of 1:1 for ethylene carbonate and diethyl carbonate (Tianjin Jinniu Power Sources Mater. Co., LTD). The cells were tested in the voltage range of 0.005～3 V with a Wuhan Land CT 2001A cycler. Cycle performance was tested at 0.1 A g^{-1}. Cyclic voltammetry (CV) was performed on a CHI760D electrochemical workstation between 0~3 V at 0.1 mV s^{-1}. Electrochemical impedance spectroscopy (EIS) was recorded with frequency set from 0.01 Hz to 100 kHz and amplitude of 5 mV [37].

3. RESULTS AND DISCUSSION

3.1 Structure and morphology of $MnFe_2O_4$ CNAs

The morphology characteristics of $MnFe_2O_4$ colloidal nanocrystal assemblies were shown in Figure 1. As depicted in the graphs, the MnFe-Na CNAs has better uniformity in particle size than MnFe-NH sample. The diameter of MnFe-Na CNAs ranges from around 150 nm to 180 nm, while, the diameter of MnFe-NH CNAs distributed mainly around 950 nm. Those values are in accord with the former reports [35,36]. The insets in Figure 1 were the selected area electron diffraction (SAED)

patterns of the two samples. It can be seen from the SAED pattern of a single MnFe-Na sphere(the inset in Figure 1a) showed widen arc-like diffraction spots forming a circular, indicating the existence of slight misalignment among the MnFe-Na primary nanocrystals [38]. The SAED pattern of MnFe-NH was small bright spots (inset in Figure 1b), denoting the highly crystallinity of the $MnFe_2O_4$ nanoparticles.

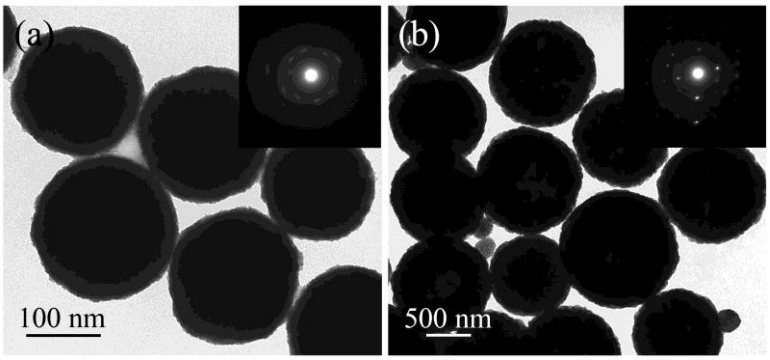

Figure 1. TEM images of the $MnFe_2O_4$ CNAs: (a) MnFe-Na; (b) MnFe-NH.

N_2 adsorption-desorption measurements were conducted for these samples. Figure 2 shows the N_2 adsorption-desorption isotherms along with the pore size distribution curves of MnFe-Na. The BET specific surface area and pore volume were respectively 123.2 m^2 g^{-1} and 0.099 cm^3 g^{-1} for MnFe-Na, while 4.14 m^2 g^{-1} and 0.015 cm^3 g^{-1} for MnFe-NH [36]. These results were in accordance with those of TEM images (Figure 1). According to the IUPAC classification, the N_2 isotherm of MnFe-Na belongs to Type IV, the hysteresis loop resemble those of Type H3. The hysteresis curves at lower relative pressure meaning the smaller pore diameter of MnFe-Na CNAs than MnFe-NH. Figure 2b indicated that the pore size distribution of MnFe-Na was about 20～55 nm smaller than that of MnFe-NH.

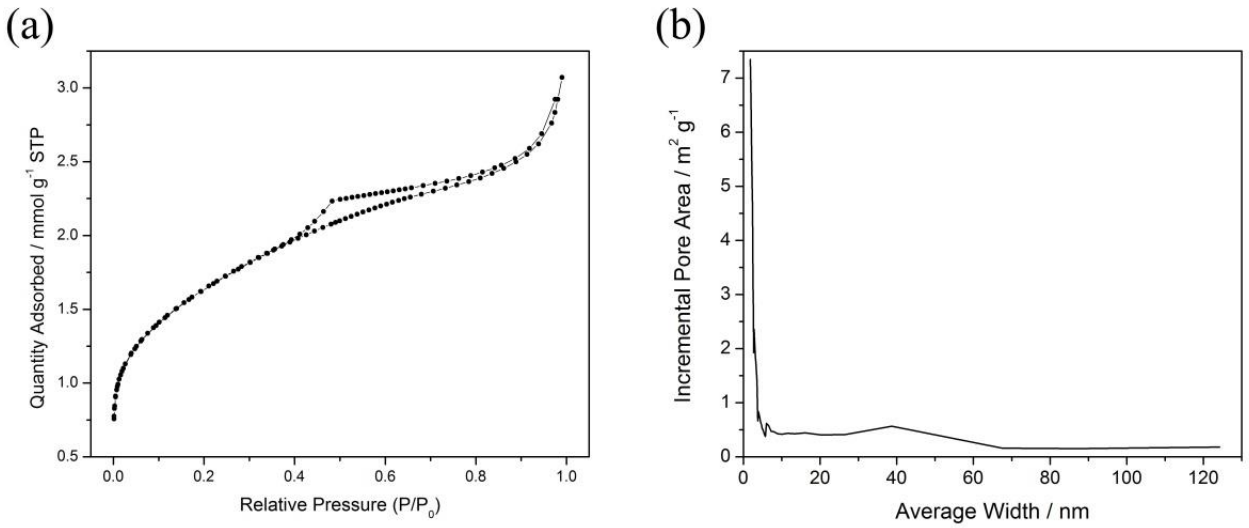

Figure 2. N_2 adsorption-desorption isotherm (a) and corresponding pore size distribution curves (b) of $MnFe_2O_4$ CNAs.

3.2 Electrochemical properties of $MnFe_2O_4$ CNAs

Figure 3 shows the charge-discharge curves of the manganese ferrite assemblyies at different current densities ranging from 0.1 A g^{-1} to 1 A g^{-1}. It is easy to see that the discharge capacities of first and second circle at 0.1 A g^{-1} was 1354.7 mAh g^{-1} and 832.8 mAh g^{-1}, 1307.0 mAh g^{-1} and 887.2 mAh g^{-1} respectively for MnFe-Na and MnFe-NH, and the discharge capacity of the two samples at 0.2 A g^{-1}, 0.5 A g^{-1} and 1 A g^{-1} was 158.3 mAh g^{-1}, 98.5 mAh g^{-1} and 59.6 mAh g^{-1}, and 229.7 mAh g^{-1}, 125 mAh g^{-1} and 77.0 mAh g^{-1}, respectively. What's more, when returns to the low current density of 0.1 A g^{-1}, the capacity of the two sample both increased to around 220 mAh g^{-1}. Besides, concludes can be draw from those data that the MnFe-NH CNAs have better rate capability than MnFe-Na.

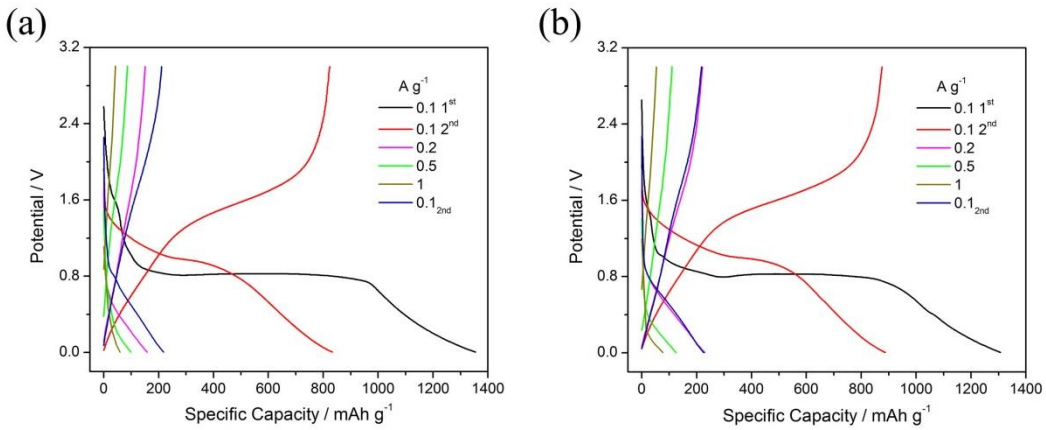

Figure 3. Charge and discharge profiles of $MnFe_2O_4$ CNAs at different current densities: (a) MnFe-Na, (b) MnFe-NH

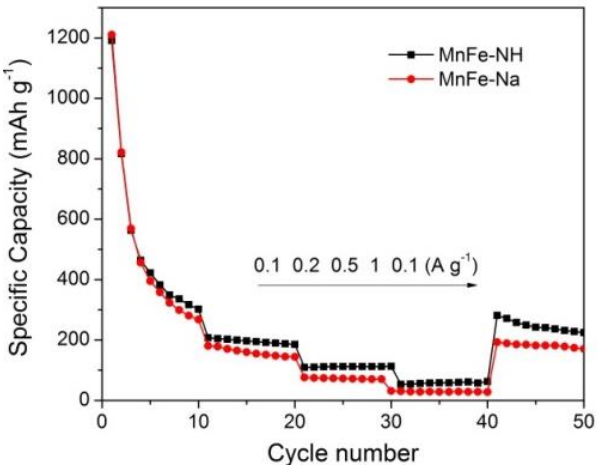

Figure 4. Rate performance of the $MnFe_2O_4$ CNAs at different current densities.

Figure 4 shows the rate properties of the manganese ferries at different current densities range from 0.1 A g^{-1} to 1 A g^{-1}. As depicted in Figure 4, the capacities of the two samples both had a sharp

decrease at 0.1 A g^{-1} in the first ten cycles from about 1200 mAh g^{-1} to 300 mAh g^{-1}, and kept relatively stable at other large current densities during the following cycles. This may be attributed to the solid electrolyte interface layer (SEI) and the large particle size that reduced the utilization of the inner crystallites. After 40 cycles, the capacities at 0.1 A g^{-1} were close to those cycled for the first time at the first ten cycles, implying good stability and reversibility of both the CNAs [39]. Moreover, the capacity of MnFe-NH was higher than that of MnFe-Na at all the experimental current densities, which can be explained by the large pore between the primary nanoparticles in MnFe-NH CNAs which may be more easier for the Li^+ ions to transfer in the active material.

Cycling properties of the two manganese ferries CNAs at 0.1 A g^{-1} were shown in Figure 5. It is clear to see that the capacities of the CNAs at 0.1 A g^{-1} maintained at about 200 mAh g^{-1} stably. The specific capacities of both the samples droped dramatically during the first ten cycles, and had slight increase after droped to the lowest value at around the 50th cycles. The increase may attribute to the better dispersity of $MnFe_2O_4$ primary nanoparticles caused by the electrochemical reactions during the charge and discharge processes, resulting in more effective contact surface between the active materials and electrolyte. What's more, the capacity of MnFe-NH kept about 45～80 mAh g^{-1} higher than the value of MnFe-Na. The probable cause may be the larger size of MnFe-NH CNAs and its large primary nanoparticles, which lead to a bigger pore for Li^+ ion to store and react with the active material.

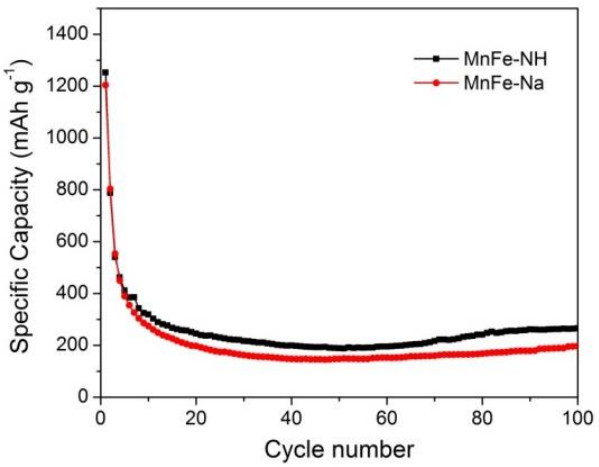

Figure 5. Cycling performance of the $MnFe_2O_4$ CNAs at 0.1 A g^{-1}.

Figure 6 shows the CV profiles of the $MnFe_2O_4$ CNAs. As shown in Figure 6a, the first circles of MnFe-NH and MnFe-Na CNAs have sharp peaks at 0.561 V and 0.605 V, respectively, which could be attributed to the formation of SEI layer and the reduction of $MnFe_2O_4$ to metallic Mn and Fe. Besides, the peak at around 1.595 V which is related to the oxidation of metallic manganese and iron to $Mn^{2+}$and Fe^{3+} [40]. These sharp redox peaks indicated the excellent charge-transfer kinetics in the begin of the electrode reaction, which is conducive to the lithium intercalation/deintercalation [41]. In the second circle (Figure 6b), both the samples have only one cathodic peak at 0.466 V and 0.526 V respectively. Besides, for the subsequent circles, there were no obvious peaks for the two $MnFe_2O_4$ CNAs, indicating the bad reversibility of the $MnFe_2O_4$ particles. It is easy to see that all peaks in the

two cycles of the MnFe-Na sample had higher peak current than that of MnFe-NH CNAs, suggesting the better cycling performance of the MnFe-Na, which is in line with the conclusion drawn from Figure 5. There were no remarkable peak in the 3rd and 4th circle of the CV plots (Figure 6c, 6d), implying the unsatisfying cycling property of these two $MnFe_2O_4$ samples

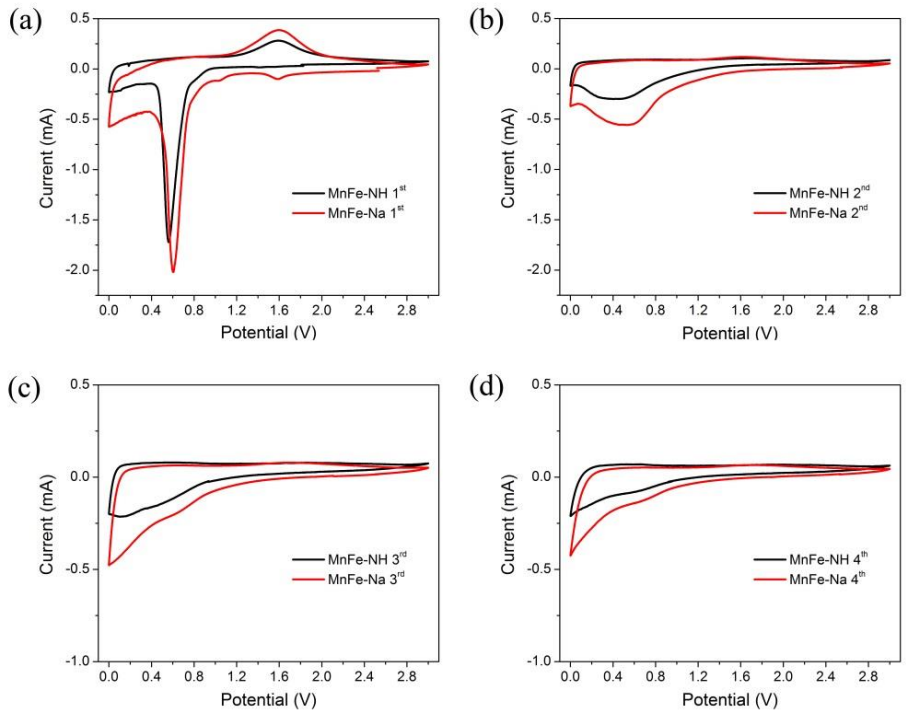

Figure 6. The CV curves of LIBs based on $MnFe_2O_4$ CNAs.

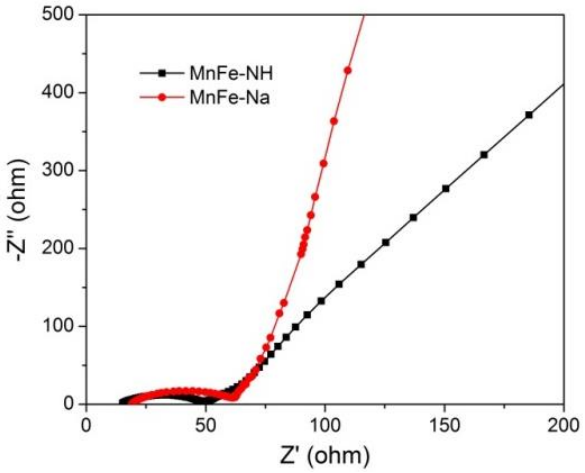

Figure 7. EIS spectra of $MnFe_2O_4$ CNAs.

To further study the electrochemical property of the $MnFe_2O_4$ CNAs, alternating current (AC) impedance technique was carried out on the CNAs at open circuit voltage. It can be seen from Figure 7 that an oblique line and a semicircle were observed in the low and high frequency range in the Nyquist plots, respectively. According to the former works [15,42], the semicircle may be resulted from the charge transfer reaction occurring at the interface of the $MnFe_2O_4$ CNAs and electrolyte, and the line

can be assigned to the Li^+ diffusion and accumulation process in the working electrode, namely Warburg resistance. As depicted in Figure 7, the semicircle diameter of the profile of MnFe-NH is smaller than that of MnFe-Na, indicating the existence of a higher electronic conductivity and smaller charge transfer resistance for MnFe-NH CNAs [40,42]. It is obvious that the slope of the line of MnFe-NH is higher than that of MnFe-Na, indicating smaller diffusion coefficient and higher Li^+ Warburg resistance [39]. These can also be attributed to the larger interspace between the primary nanoparticles in MnFe-NH CNAs.

4. CONCLUSION

In a word, $MnFe_2O_4$ colloidal nanocrystal assemblies with different sizes were synthesized though solvothermal approach, which were obtained by the in-situ self-assembly of primary $MnFe_2O_4$ nanoparticles. The electrochemical measurements showed that the larger nanoparticle in $MnFe_2O_4$ CNAs is good for the storage and intercalation/deintercalation of lithium, which resulted in higher specific capacity and better cycling properties of the MnFe-NH CNAs. Moreover, the EIS spectra indicated that the sample MnFe-NH had higher electronic conductivity and smaller diffusion coefficient compared with sample MnFe-Na. These conclusions suggested the promising prospect of $MnFe_2O_4$ as anode materials for lithium-ion batteries and the particle size plays an important role in its electrochemical properties.

ACKNOWLEDGMENTS
This work was financially supported by the National Natural Science Foundation of China (No. 21143006 and U1232104) , the Qingdao Livelihood of Science and Technology Plan Project (No. 15-9-2-118-nsh), the Qingdao Postdoctoral Application Research Project (No. 2015135), the National Spark Plan Project (No. 2015GA741009) and the Foundation of “Taishan Scholar” program of Shandong Province, China.

Reference

1. W. Wei, Z. Wang, Z. Liu, Y. Liu, L. He, D. Chen, A. Umar, L. Guo, J. Li. *J.Power Sources*, 238 **(**2013), 376.
2. C. Liang, M. Gao, H. Pan, Y. Liu, M. Yan. 575 **(**2013), 246.
3. Y.F. Deng, S.D. Tang, Q.M. Zhang, Z. Shi, L. Zhang, S.Z. Zhan, G.H. Chen. *J. Mater. Chem.*, 21 **(**2011), 11987.
4. C.J. Chen, M. Greenblatt, J.V. Waszczak. *Solid State Ionics*, 18-19 **(**1986), 838.
5. M. Armand, J.M. Tarascon. *Nature*, 451 **(**2008), 652.
6. A.W. Anwar, A. Majeed, N. Iqbal, W. Ullah, A. Shuaib, U. Ilyas, F. Bibi, H.M. Rafique. *J. Mater. Sci. Technol.*, 31 **(**2015), 699.
7. Z.H. Li, T.P. Zhao, X.Y. Zhan, D.S. Gao, Q.Z. Xiao, G.T. Lei. *Electrochim. Acta*, 55 **(**2010), 4594.
8. A. Dhanabalan, X. Li, R. Agrawal, C. Chen, C. Wang. *Nanomaterials*, 3 **(**2013), 606.
9. X. Yao, C. Tang, G. Yuan, P. Cui, X. Xu, Z. Liu. *Electrochem. Commun.*, 13 **(**2011), 1439.
10. Z. An, J. Zhang, S. Pan. *Mater. Res. Bull.*, 47 **(**2012), 3976.
11. S. Ni, T. Li, X. Lv, X. Yang, L. Zhang. *Electrochim. Acta*, 91 **(**2013), 267.

12. Kang Wen, Guanghui Chen, Feng Jiang, Xiangyang Zhou, J. Yang. *Int. J. Electrochem. Sci.*, 10 **(**2015), 3859.
13. O. Waser, M. Hess, A. Güntner, P. Novák, S.E. Pratsinis. *J.Power Sources*, 241 **(**2013), 415.
14. N. Wang, H. Xu, L. Chen, X. Gu, J. Yang, Y. Qian. *J.Power Sources*, 247 **(**2014), 163.
15. Y. Pan, Y. Zhang, X. Wei, C. Yuan, J. Yin, D. Cao, G. Wang. *Electrochim. Acta*, 109 **(**2013), 89.
16. S. Liu, J. Wu, J. Zhou, G. Fang, S. Liang. *Electrochim. Acta*, 176 **(**2015), 1.
17. Y. Chen, J. Zhu, B. Qu, B. Lu, Z. Xu. *Nano Energy*, 3 **(**2014), 88.
18. B.S. Randhawa, J. Singh, H. Kaur, M. Kaur. *Ceram. Int.*, 36 **(**2010), 1993.
19. R. Alcantara, M. Jaraba, P. Lavela, J.L. Tirado, J.C. Jumas, J. Olivier-Fourcade. *Electrochem. Commun.*, 5 **(**2003), 16.
20. H. Liu, H. Zhu, H. Yang. *Mater. Res. Bull.*, 48 **(**2013), 1587.
21. N. Wang, X. Ma, H. Xu, L. Chen, J. Yue, F. Niu, J. Yang, Y. Qian. *Nano Energy*, 6 **(**2014), 193.
22. R. Jin, H. Liu, Y. Guan, J. Zhou, G. Chen. *Mater. Lett*., 158 **(**2015), 218.
23. LinLin Wang, ZhiPeng Wu, Kaibin Tang, XiaoZhu Zhang, Min Zhang, DaoLi Zhao, J. Xu. *Int. J. Electrochem. Sci.*, 10 **(**2015), 6714
24. L. Yao, X. Hou, S. Hu, J. Wang, M. Li, C. Su, M.O. Tade, Z. Shao, X. Liu. *J.Power Sources*, 258 **(**2014), 305.
25. Y.-N. NuLi, Q. Z. Qin. *J.Power Sources*, 142 **(**2005), 292.
26. J. Cabana, L. Monconduit, D. Larcher, M. Rosa Palacin. *Adv. Mater.*, 22 **(**2010), E170.
27. L. Duan, Y. Wang, L. Wang, F. Zhang, L. Wang. *Mater. Res. Bull.*, 61 **(**2015), 195.
28. P. Ramesh Kumara, S. Mitra. *RSC Adv.*, 3 **(**2013), 25058.
29. Z. Xing, Z. Ju, J. Yang, H. Xu, Y. Qian. *Electrochim. Acta.*, 102 **(**2013), 51.
30. L. Luo, R. Cui, H. Qiao, K. Chen, Y. Fei, D. Li, Z. Pang, K. Liu, Q. Wei. *Electrochim. Acta.*, 144 **(**2014), 85.
31. X. Guo, X. Lu, X. Fang, Y. Mao, Z. Wang, L. Chen, X. Xu, H. Yang, Y. Liu. *Electrochem. Commun.*, 12 **(**2010), 847.
32. F.M. Courtel, Y. Abu-Lebdeh, I.J. Davidson. *Electrochim. Acta.*, 71 **(**2012), 123.
33. Y. Wang;, G.Z. Cao. *Adva. Mater.*, 20 **(**2008), 2251.
34. A.S. Arico, P. Bruce, B. Scrosati, J.M. Tarascon, W. VanSchalkwijk. *Nat. Mater*., 4 **(**2005), 366.
35. P. Guo, G. Zhang, J. Yu, H. Li, X.S. Zhao. *Colloid. Surf. A.*, 395 **(**2012), 168.
36. Zhen Li, Kai Gao, Guangting Han, Rongyue Wang, Hongliang Li, X. S. Zhao, P. Guo. *New J. Chem.*, 39 **(**2015), 361.
37. F.F. Leng, X. Yan, L.Y. Jing, R.R. Liu, Y.Z. Long, H.L. Li, X.S. Zhao, P.Z. Guo, Colloids Surf. A, 495 (2016), 54.
38. J.P. Ge, Y. Hu, M. Biasini, W.P. Beyermann, Y.D. Yin. *Angew. Chem. Int. Ed.*, 46 **(**2007), 4342.
39. G. Wang, H. Wang, J. Bai. *J. Alloy. Compd.*, 627 **(**2015), 174.
40. Songmei Li, Bo Wang, Bin Li, Jianhua Liu, Mei Yu, X. Wu. *Mater. Res. Bull*., 61 **(**2015), 369.
41. R.M. Thankachan, M.M. Rahman, I. Sultana, A.M. Glushenkov, S. Thomas, N. Kalarikkal, Y. Chen. *J.Power Sources*., 282 **(**2015), 462.
42. José R. González, Ricardo Alcántara , Francisco Nacimiento, J.L. Tirado. *J. Solid State Electrochem.*, 17 **(**2013), 2495.
43. Y. Shao, M. Engelhard, Y. Lin. *Electrochem. Commun.*, 11 **(**2009), 2064.